A Customized EKF model for GNSS-based Navigation in the Harsh Space Environment

A Customized EKF model for GNSS-based Navigation in the Harsh Space Environment

Oliviero Vouch*, Andrea Nardin*, Alex Minetto*, Matteo Valvano*, Simone Zocca*, Fabio Dovis*
*Department of Electronics and Telecommunications (DET), Politecnico di Torino, Torino, Italy

***Abstract*—The extension of the Global Navigation Satellite System (GNSS) Space Service Volume (SSV) is of utmost relevance to afford enhanced autonomy in navigation, guidance, and control of space missions. Pioneering studies have shown the feasibility of using terrestrial GNSS signals in space applications, supporting Orbit Determination and Time Synchronization (ODTS) during Earth-Moon transfer orbits (MTOs) and lunar landings. However, non-terrestrial applications face challenges due to compromised signal availability at high altitudes, thus requiring advanced receiver architectures coupled with external aiding data. This paper presents a customized Bayesian filter, the Trajectory-Aware Extended Kalman Filter (TA-EKF), specifically designed for GNSS navigation along MTOs. The proposed filter architecture integrates aiding information, such as the planned mission orbital trajectory, to speed up filter convergence and achieve highly accurate positioning solutions. The performance of the TA-EKF is evaluated through simulations of MTO mission scenarios supported by Monte Carlo analyses, and it is compared against a standalone EKF.**

***Index Terms*—Global Navigation Satellite System, Moon, Space Service Volume, Lunar Missions, Extended Kalman Filter**

I. Introduction

Although Global Navigation Satellite Systems (GNSSs) were historically conceived to supply accurate and dependable Positioning, Navigation and Timing (PNT) to terrestrial users, the momentum taken by the space sector has made the space environment a new playground for in-orbit GNSS-based navigation systems. Since the Global Positioning System Package (GPSPAC) onboard the Landsat 4 mission was launched in 1982 [1], major technology progress in GNSS space-borne receivers allowed to steadily improve the spectrum of PNT services within the Terrestrial Service Volume (TSV) [2]. Over the past decade, the increasing demand for navigation capability for space vehicles has fostered the expansion of the Space Service Volume (SSV) well beyond the Low-Earth Orbit (LEO) [3]. Interestingly, National Aeronautics and Space Administration (NASA)'s Magnetospheric Multiscale Mission (MMS) set the highest record for GNSS signal reception and onboard Position, Velocity, Timing (PVT) solutions to about $150\,000\,\mathrm{km}$, i.e., ~ 25 Earth Radii (RE), away from the Earth's surface [4]. Nevertheless, most of state-of-the-art Orbit Determination and Time Synchronization (ODTS) and Precise Orbit Determination (POD) algorithms are still broadly relying on Direct-to-Earth (DTE) ranging capabilities and long-term post-processing solutions [5], [6]. These methods, besides putting high costs on the ground infrastructure, might turn out not being sufficient to support the deep-space exploration roadmap both in terms of service availability and far-side accessibility [7], [8].

Forecasting a sustained human presence to the Moon for long-term operations on the lunar surface and at other deep space destinations, increased autonomy in high-altitude spacecraft navigation and guidance is urgent [9]. Further motivated by the absence of a dedicated communication and navigation infrastructure in the lunar environment, Earth GNSS signals are key to enable real-time absolute positioning for Earth-Moon transfer orbits (MTOs) as well as to assist in Moon landing operations [10]–[12]. However, the MTO environment poses non-trivial challenges that can prevent the navigation unit from achieving highly-accurate orbit determination. In fact, reduced GNSS signal availability is likely to be experienced at high altitudes because of the very-limited region in the field of view where satellites can be observed [11]. In addition, the unfortunate distribution of GNSS satellites can result in very-high Geometric Dilution Of Precision (GDOP), even with multi-constellation GNSS receiver processing. Indeed, the steady spacecraft dynamics along the MTO penalises spatial diversity in the retrieved satellite measurements, thus increasing their linear dependency in multilateration problems. Against this background, a batch Least-Mean Squares (LMS) estimator inevitably leads to extremely coarse single-point solutions, even if the receiver could process satellite signals correctly and provide sufficient observables. Moreover, filtered GNSS navigation solutions obtained through legacy Bayesian formulations [13], [14] can be affected by errors of hundreds of meters when approaching Moon altitudes. Yet the moderate accuracy improvements obtained from the combined processing of both code-based and carrier phase-based observables are not rewarding the increased burden of handling phase-cycle ambiguities [15].

A well-documented approach to pursue precise satellite orbit determination foresees the integration of an orbital propagator within the GNSS navigation filter [16], [17]. Being the spacecraft trajectory constrained by the orbital forces, GNSS observations can be tightly fused with an orbital forces' model; while the latter is used to propagate the spacecraft's state along its orbit, satellite measurements can prevent the orbital

This study was funded within the contract n. 2021-26-HH.0 ASI/Politecnico di Torino "Attività di R&S inerente alla Navigazione GNSS nello Space volume Terra/Luna nell'ambito del Lunar GNSS Receiver Experiment". O. Vouch acknowledges funding from the Politecnico di Torino Interdepartmental Centre for Service Robotics (PIC4SeR). A. Minetto acknowledges funding from the research contract no. 32-G-13427-5 DM 1062/2021 funded within the Programma Operativo Nazionale (PON) Ricerca ed Innovazione of the Italian Ministry of University and Research (MUR).

propagation from drifting. The resulting hybrid architecture is often referred to as Orbital Filter (OF), and the work in [18] was a pioneering Proof of Concept (PoC) of an OF for the MTO based on an Extended Kalman Filter (EKF).

In a similar vein, this contribution proposes a customized EKF architecture tailored to GNSS-based navigation on the way to the Moon. The developed solution, namely a Trajectory-Aware EKF (TA-EKF), integrates the information about the planned MTO as an aiding to correct the EKF state-prediction which follows an oversimplified constant-velocity process model. By leveraging a dedicated simulation framework able to faithfully reproduce the GNSS signal environment up to Moon altitudes, the TA-EKF is verified against a plain EKF architecture. In particular, Monte Carlo (MC) analyses allow to exhaustively investigate the TA-EKF positioning accuracy performance together with its convergence pattern.

II. Background

Following the Bayesian approach to statistical estimation, the process to be estimated and the associated dependency of measurements may be written in the form [19]:

$$\boldsymbol{x}_k = \boldsymbol{f}_{k-1}(\boldsymbol{x}_{k-1}, \boldsymbol{u}_{d,k-1}) + \boldsymbol{w}_{k-1} \tag{1}$$

$$\boldsymbol{z}_k = \boldsymbol{h}_k(\boldsymbol{x}_k) + \boldsymbol{v}_k \tag{2}$$

where:

- $\boldsymbol{x}_k$ is the true, unknown process state at time t_k;
- $\boldsymbol{z}_k$ is the deterministic measurement vector at time t_k;
- $\boldsymbol{w}_{k-1} \sim \mathcal{N}(\boldsymbol{0}, \boldsymbol{Q}_{k-1})$ and $\boldsymbol{v}_k \sim \mathcal{N}(\boldsymbol{0}, \boldsymbol{R}_k)$ are the normally distributed process and measurement noises, respectively; they are assumed with zero-mean, known variance-covariance statistics and mutually independent.
- $\boldsymbol{f}_{k-1}$ and $\boldsymbol{h}_k$ are known, non-linear state-transition and observation functions, respectively.
- $\boldsymbol{u}_{d,k-1}$ are deterministic forcing functions affecting the process state; this term is assumed equal to zero.

The combination of (1) and (2) leads to a state-space formulation following a Hidden Markov Model (HMM) [20]. Identifying with $\boldsymbol{x}_k^*$ the estimated process state at time t_k—which includes, among the other quantities, the spacecraft trajectory—the following relation holds:

$$\boldsymbol{x}_k = \boldsymbol{x}_k^* + \Delta\boldsymbol{x}_k \tag{3}$$

which introduces $\Delta\boldsymbol{x}_k$ as the residual of the estimate. Choosing $\boldsymbol{x}_k^* = \boldsymbol{f}_{k-1}(\boldsymbol{x}_{k-1}^*)$, the linear(-ized) process dynamics and measurement models can be obtained in terms of residuals [19]:

$$\Delta\boldsymbol{x}_k = \boldsymbol{\Phi}_{k-1} \cdot \Delta\boldsymbol{x}_{k-1} + \boldsymbol{w}_{k-1} \tag{4}$$

$$\boldsymbol{z}_k - \boldsymbol{h}_k(\boldsymbol{x}_k^*) = \boldsymbol{H}_k \cdot \Delta\boldsymbol{x}_k + \boldsymbol{v}_k \tag{5}$$

where $\boldsymbol{\Phi}_{k-1}$ and $\boldsymbol{H}_k$ are the linear(-ized) state-transition matrix and measurement matrix, respectively. Based on model (4), the predicted residual takes the form:

$$\Delta\hat{\boldsymbol{x}}_k^- = \boldsymbol{\Phi}_{k-1} \cdot \Delta\hat{\boldsymbol{x}}_{k-1} \tag{6}$$

being $\Delta\hat{\boldsymbol{x}}_{k-1}$ the residual on the last process estimate at t_{k-1}. Summing $\boldsymbol{x}_k^*$ on both sides of (6), the linear(-ized) process prediction model in terms of total states reads as [19]:

$$\underbrace{\boldsymbol{x}_{\boldsymbol{k}}^* + \Delta\hat{\boldsymbol{x}}_k^-}_{\hat{\boldsymbol{x}}_{\boldsymbol{k}}^-} = \boldsymbol{\Phi}_{k-1} \cdot \left(\underbrace{\boldsymbol{x}_{k-1}^* + \Delta\hat{\boldsymbol{x}}_{k-1}}_{\hat{\boldsymbol{x}}_{k-1}} \right) \tag{7}$$

with the associated predicted process covariance:

$$\hat{\boldsymbol{P}}_k^- = \boldsymbol{\Phi}_{k-1}\hat{\boldsymbol{P}}_{k-1}\boldsymbol{\Phi}_{k-1}^T + \boldsymbol{Q}_k. \tag{8}$$

Accordingly, leveraging on model (5), the corrected residual estimate at time t_k follows as:

$$\Delta\hat{\boldsymbol{x}}_{\boldsymbol{k}} = \Delta\hat{\boldsymbol{x}}_k^- + \boldsymbol{K}_k \left[\boldsymbol{z}_k - \underbrace{\left(\boldsymbol{h}_k(\boldsymbol{x}_k^*) + \boldsymbol{H}_k\Delta\hat{\boldsymbol{x}}_{\boldsymbol{k}}^- \right)}_{\hat{\boldsymbol{z}}_{\boldsymbol{k}}^-} \right] \tag{9}$$

where the predicted measurements $\hat{\boldsymbol{z}}_k^-$ are highlighted. Eventually, the linear(-ized) process update equation in terms of total states is obtained from (9) by resuming $\boldsymbol{x}_k^*$ [19]:

$$\underbrace{\boldsymbol{x}_{\boldsymbol{k}}^* + \Delta\hat{\boldsymbol{x}}_{\boldsymbol{k}}}_{\hat{\boldsymbol{x}}_{\boldsymbol{k}}} = \hat{\boldsymbol{x}}_k^- + \boldsymbol{K}_k(\boldsymbol{z}_{\boldsymbol{k}} - \hat{\boldsymbol{z}}_{\boldsymbol{k}}^-) \tag{10}$$

The associated process covariance update is:

$$\hat{\boldsymbol{P}}_k = (\boldsymbol{I} - \boldsymbol{K}_k\boldsymbol{H}_k)\hat{\boldsymbol{P}}_k^-(\boldsymbol{I} - \boldsymbol{K}_k\boldsymbol{H}_k)^T + \boldsymbol{K}_k\boldsymbol{R}_k\boldsymbol{K}_k^T \tag{11}$$

being $\boldsymbol{K}_k = \hat{\boldsymbol{P}}_k^-\boldsymbol{H}_k^T(\boldsymbol{H}_k\hat{\boldsymbol{P}}_k^-\boldsymbol{H}_k^T + \boldsymbol{R}_k)^{-1}$ the Kalman gain.

A. Transitional model for process dynamics

Although a plethora of possibilities exist [21], a simple constant velocity model is selected to characterize the discrete-time evolution of the process state. Then, the state vector at time t_k is defined as:

$$\boldsymbol{x}_k = \begin{bmatrix} \boldsymbol{r}_k & \boldsymbol{v}_k & b_k & \dot{b}_k \end{bmatrix}^T \tag{12}$$

and it involves the following quantities:

- $\boldsymbol{r}_k$ the spacecraft antenna absolute position vector (Earth-Centred Earth-Fixed (ECEF) coordinates) in (m);
- $\boldsymbol{v}_k$ the spacecraft antenna absolute velocity vector (ECEF coordinates) in $(\mathrm{m/s})$;
- b_k the range equivalent of the GNSS receiver clock offset in (m);
- $\dot{b}_k$ the range-rate equivalent of the GNSS receiver clock drift in $(\mathrm{m/s})$;

Based on (12), the state-transition matrix corresponds to [22]:

$$\boldsymbol{\Phi}_{k-1} = \begin{bmatrix} \boldsymbol{I}_{3\times3} & \boldsymbol{I}_{3\times3}\Delta t & \boldsymbol{0}_{3\times1} & \boldsymbol{0}_{3\times1} \\ \boldsymbol{0}_{3\times3} & \boldsymbol{I}_{3\times3} & \boldsymbol{0}_{3\times1} & \boldsymbol{0}_{3\times1} \\ \boldsymbol{0}_{1\times3} & \boldsymbol{0}_{1\times3} & 1 & \Delta t \\ \boldsymbol{0}_{1\times3} & \boldsymbol{0}_{1\times3} & 0 & 1 \end{bmatrix} \tag{13}$$

where Δt is the process state propagation interval, $\boldsymbol{I}_{n\times n}$ is the $n \times n$ identity matrix and $\boldsymbol{0}_{n\times n}$ is the $n \times n$ null-matrix.

Eventually, the process noise variance-covariance matrix can be compactly written as [22]:

$$\boldsymbol{Q}_{k-1} = \begin{bmatrix} \boldsymbol{Q}_p & \boldsymbol{0}_{6\times 2} \\ \boldsymbol{0}_{2\times 6} & \boldsymbol{Q}_t \end{bmatrix} \tag{14}$$

where $\boldsymbol{Q}_p$ is the covariance component for the positioning states resolved about the ECEF-frame axes; it reads as:

$$\boldsymbol{Q}_p = \begin{bmatrix} \frac{\Delta t^3}{3} & \frac{\Delta t^2}{2} \\ \frac{\Delta t^2}{2} & \Delta t \end{bmatrix} \otimes diag(\underbrace{S_{a,x}, S_{a,y}, S_{a,z}}_{\boldsymbol{S}_a}) \tag{15}$$

being $\boldsymbol{S}_a$ the acceleration Power Spectral Density (PSD) and $\otimes$ the Kronecker product. Similarly, $\boldsymbol{Q}_t$ is the covariance component for the timing states and equals:

$$\boldsymbol{Q}_t = \begin{bmatrix} S_{c\phi}\Delta t + S_{cf}\frac{\Delta t^3}{3} & S_{cf}\frac{\Delta t^2}{2} \\ S_{cf}\frac{\Delta t^2}{2} & S_{cf}\Delta t \end{bmatrix} \tag{16}$$

being $S_{c\phi}$ and S_{cf} the PSDs of the GNSS receiver clock phase-drift and frequency-drift, respectively[1].

III. Methodology

A. Trajectory-Aware EKF for MTO navigation

According to the developed TA-EKF model, the GNSS navigation filter is aided by the nominal spacecraft trajectory along the MTO. The latter trajectory—in terms of spacecraft position and velocity—can be retrieved onboard as an *aiding state* via

- Guidance, Navigation & Control (GNC) subsystems;
- processing of radiometric measurements - performed at the mission ground segment by federated ground-based networks and uploaded as telecommands [6] - paired with a suitable propagator.

This aiding to the GNSS navigation filter is meant to enhance the process state prediction as well as to empower the filter convergence rate upon initialization. By identifying with $\tilde{\boldsymbol{x}}_{k-1}$ the aiding state the latest a-posteriori estimate $\hat{\boldsymbol{x}}_{k-1}$ is mapped to, a residual term can be defined:

$$\boldsymbol{\varepsilon}_{k-1} = \hat{\boldsymbol{x}}_{k-1} - \tilde{\boldsymbol{x}}_{k-1}. \tag{17}$$

Then, the linear(-ized) prediction model (7) can be modified in order to account for the residual term:

$$\hat{\boldsymbol{x}}_k^- = \boldsymbol{\Phi}_{k-1}\hat{\boldsymbol{x}}_{k-1} - \boldsymbol{\varepsilon}_{k-1}. \tag{18}$$

For this approach to be effective, accurate synchronization must exist between $\hat{\boldsymbol{x}}_{k-1}$ and the aiding state it is mapped to via (17). Suppose the aiding describing the nominal process state evolution is given as a discrete-time sequence of state vectors. Given the generic $k-1$-th time instant and in the absence of any additional timing information, it is not obvious which aiding state vector should be matched to $\hat{\boldsymbol{x}}_{k-1}$. In fact, there is no guarantee that a one-to-one sample matching between the aiding and the estimated trajectories is optimal. Accordingly, several strategies can be implemented to perform aiding matching [24]. For example, one might select the aiding state upon interpolation of the available data, taking into account both the elapsed time as well as potential receiver motion anomalies that might cause abrupt slowdowns and accelerations [25]. Given the same sample rate between the nominal spacecraft trajectory and the GNSS navigation filter estimate, in this work the aiding state is selected by averaging over a set of aiding state vectors taken within a neighborhood of $\hat{\boldsymbol{x}}_{k-1}$. Overall, the more the identification of the aiding state is accurate, the faster is expected to be the navigation filter convergence.

B. Simulation framework

As a byproduct of ongoing research activities, the upcoming Lunar GNSS Receiver Experiment (LuGRE) is taken as reference mission-case scenario. LuGRE is a joint NASA-Italian Space Agency (ASI) demonstration payload which will be carried on the Firefly Blue Ghost Mission 1 (BGM1) with the goal of demonstrating multi-GNSS based PNT in cis-lunar space and at Moon altitudes [26], [27]. Among the driving scientific investigations identified to respond to the LuGRE objectives, it is considered the performance assessment of filtering-based PVT solutions obtained both onboard throughout the mission and via ground-based post-processing of the multi-GNSS observables collected during the mission transit-phase up to Moon altitudes (i.e., about 62 RE) [28].

Tailored to this case-study, a custom Matlab®-based software simulator has been developed in order to emulate the GNSS signal environment experienced along the MTO. Two GNSS constellations are considered: Global Positioning System (GPS) and Galileo. As regards the former, the antenna panel patterns for Block IIR and IIR-M satellites have been designed following the technical documentation released by the U.S. Coast Guard Navigation Center (NAVCEN) [29]. Moreover, details about the panel pattern specification for Block IIF over L1-band was retrieved based on the published scientific products from NASA's GPS Antenna Characterization Experiment (GPS ACE) [30]. Concerning Galileo satellites' antenna radiation patterns, the details of which are kept confidential, unofficial Effective Isotropic Radiated Power (EIRP) values have been assumed for main and side lobes as derived by the European Space Operations Centre (ESOC) to enable preliminary scientific investigations in support of the PROBA-3 mission [31]. For the radiation patterns of both constellations, a 90° off-boresight angle mask is adopted.

1) Modelling and simulation of GNSS observables: In the designed simulation framework, the synthetic generation of GNSS observables to each of the modelled GPS and Galileo satellites along the MTO is bound to both geometric and radiometric visibility conditions. In particular, geometric visibility takes into account the instantaneous availability of a Line-of-Sight (LOS) link between the spacecraft and the satellite vehicle; it can be hindered either in case the satellite-spacecraft baseline is more than 90° off-boresight the nadir pointing

[1]For $\boldsymbol{Q}_{k-1}$, $S_{c\phi} = 2.5\cdot 10^{-12}$ (m/s)^2/Hz, $S_{cf} = 1.5\cdot 10^{-4}$ (m/s^2)^2/Hz, $S_{a,x} = S_{a,y} = S_{a,z} = 2$ (m/s^2)^2/Hz were set as in [23].

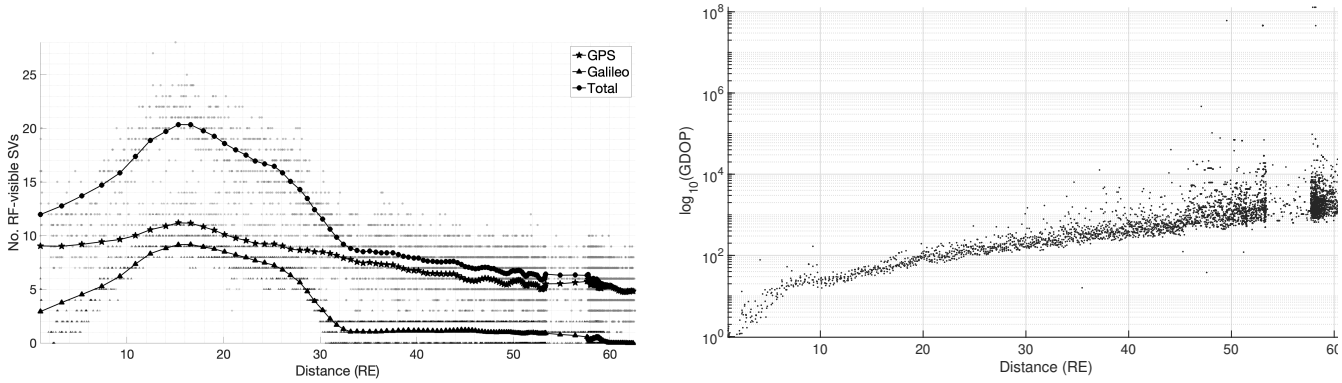

(a) (b)

Fig. 1: Expected radiometric visibility pattern for both GPS and Galileo constellations (a) and GDOP profile (b) along the MTO up to low-lunar orbit.

direction, or as a result of occultation effects induced by the Earth and the Moon. Radiometric visibility, instead, is based upon the estimation of the received Carrier-to-Noise-density ratio (C/N_0) from each satellite, and it leverages the link-budget equation modelling the C/N_0 obtained by the LuGRE receiver [26]. Radiometric visibility strictly depends on a favourable alignment of the receiver's and GNSS satellites' antenna radiation patterns.

Pseudorange measurements carry satellites-to-spacecraft range information corrupted by satellite clock errors, propagation delays induced by the atmosphere, plus other unmodelled effects usually lumped into a residual error term [32]. For simulation purposes, only code-based ranging is considered and compensation of the modelled bias contributions is assumed. Therefore, the corrected pseudorange measurement to a visible satellite s at time instant t_k is simulated according to:

$$P_{r,k}^{(s)} = \rho_{r,k}^{(s)} + \underbrace{c\delta t_{r,k}}_{b_k} + \epsilon_{r,k}^{(s)} \tag{19}$$

where:

- $\rho_{r,k}^{(s)}$ is the spacecraft-to-satellite geometric range in (m);
- $\delta t_{r,k}$ is the spacecraft GNSS receiver clock offset in (s);
- $\epsilon_{r,k}^{(s)} \sim \mathcal{N}\left(0, \sigma_{r,k}^{(s)}\right)$ is the normally distributed pseudorange residual in (m).

For $\delta t_{r,k}$, the apex (s) is omitted in (19) under the hypothesis that satellite measurements are predicted forward to a time of arrival common to all active receiver tracking channels (i.e., t_k); it follows that the receiver clock bias evenly affects all the available observables. Accounting for the phase noise on the clock offset and the random walk of the receiver clock drift over Δt, $\delta t_{r,k}$ is simulated according to:

$$\delta t_{r,k} = \underbrace{\sqrt{\frac{S_{c\phi}}{\Delta t} + \frac{S_{cf}\Delta t}{3}}}_{\bar{\boldsymbol{x}}_{\phi,rms}} + \mathcal{N}\left(0, S_{cf}\Delta t\right) \tag{20}$$

where $\bar{\boldsymbol{x}}_{\phi,rms}$ is the average Root-Mean-Square (RMS) value for the clock offset phase noise. As concerns $\epsilon_{r,k}^{(s)}$, the value of $\sigma_{r,k}^{(s)}$ is computed as a function of the estimated C/N_0 following the model reported in [27].

The corrected Doppler-shift measurement, transformed into the equivalent pseudorange-rate, to a visible satellite s at time instant t_k is constructed based on the radial component of the satellite-spacecraft relative velocity vector:

$$\dot{P}_{r,k}^{(s)} = \boldsymbol{u}_{r,k}^{(s)^T}\left[\boldsymbol{v}_k^{(s)} - \boldsymbol{v}_k\right] + \dot{b}_k + \dot{\epsilon}_{r,k}^{(s)} \tag{21}$$

where:

- $\boldsymbol{v}_k^{(s)}$ is the velocity vector of visible satellite (s) at the measured transmission time (w.r.t. t_k) in $(\mathrm{m/s})$;
- $\boldsymbol{u}_{r,k}^{(s)}$ is the spacecraft-to-satellite unit LOS vector;
- $\dot{\epsilon}_{r,k}^{(s)}$ is the normally distributed pseudorange-rate residual (i.e., $\dot{\epsilon}_{r,k}^{(s)} \sim \mathcal{N}\left(0, \dot{\sigma}_{r,k}^{(s)}\right)$) in $(\mathrm{m/s})$.

Similarly to $\epsilon_{r,k}^{(s)}$, the value of $\dot{\sigma}_{r,k}^{(s)}$ for $\dot{\epsilon}_{r,k}^{(s)}$ is retrieved as a function of the estimated C/N_0 following the corresponding model in [27].

IV. Results

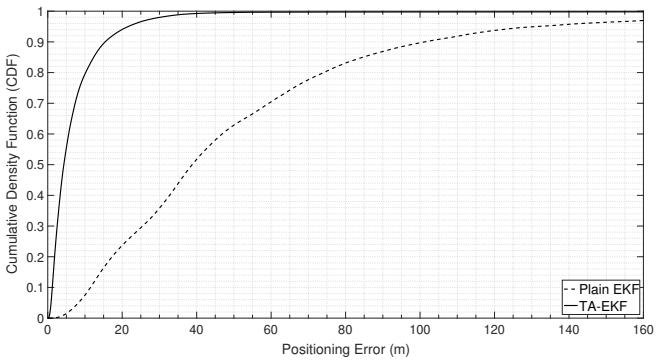

Fig. 2: Empirical CDF (ECDF) lines of the positioning error in ECEF-coordinates. Comparison between plain EKF and TA-EKF.

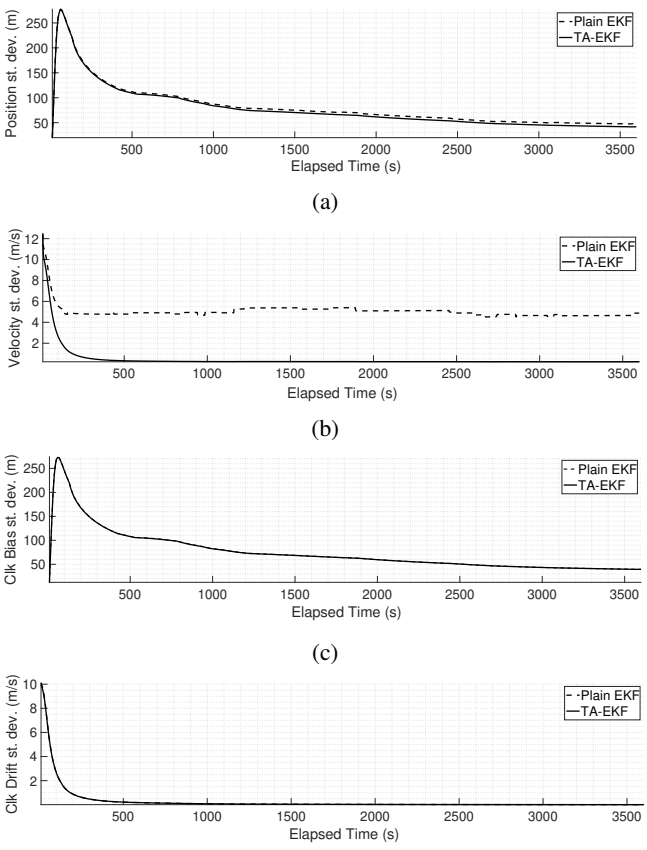

Fig. 3: Time-series of the standard deviation (1σ) of the navigation filter estimates for the position (a), velocity (b), clock-bias (c) and clock-drift (d) states. Comparison between plain EKF and TA-EKF.

A. Predicted visibility and dilution of precision throughout MTO

Taking a reference C/N_0 threshold of 23 dBHz to discriminate radiometric visibility of satellites, Fig. 1a reports the predicted signal availability as a function of the distance from the Earth (in RE) along the MTO. In particular, both composite and disjoint trends are shown for GPS and Galileo constellations. GNSS Observables are available if either geometric and radiometric visibility are experienced at the receiver location. Line markers represent the average number of GNSS satellites under radiometric visibility measured over 15-minutes long time windows during the simulated mission transit-phase. Moreover, background markers highlight that, besides the mean expected radiometric visibility, instantaneous satellite visibility might be oscillating. Interestingly, the Galileo constellation shows a much earlier average radiometric visibility drop-off at about 30 RE compared to the GPS constellation. This phenomenon is likely to be induced by an overly pessimistic assumption for the EIRP values of both main and side lobes of Galileo satellites' radiation patterns.

The estimated GDOP profile along the MTO is represented in Fig. 1b. Unsurprisingly, the more the spacecraft gets away from the Earth's surface, the more the GDOP deteriorates. In fact, close to the Earth, radiometric-visible satellites fall under a broader angle of view which generally guarantees a low linear dependency among the spacecraft-to-satellite unit LOS pointing vectors; on the contrary, getting away from the earth's surface, the angle of view increasingly narrows whichever the satellite distribution is and the geometrical arrangement of ranging sources deteriorates. This phenomenon is summarized by the resulting GDOP profile which acts as a compact, although non-exhaustive, scalar indicator of the effect of the satellites' spatial distribution on the covariance terms of the state estimates.

B. Navigation filters comparison

With the aim of statistically assessing the state-estimation performance of the proposed TA-EKF architecture, a mission time frame of one hour is selected in a neighborhood of a point belonging to the LuGRE trajectory at about 25 RE. In fact, this portion of the LuGRE MTO is considered relevant to the mission scientific objectives [26]. Fig. 2 illustrates the Empirical Cumulative Density Function (ECDF) of the positioning error obtained via MC analysis with 100 runs. Moreover, Table I summarizes the cumulative statistics at few relevant percentiles. Taking the accuracy as figure of merit, the proposed TA-EKF architecture achieves obvious gains over a plain EKF. For example, at the 95-th percentile, the accuracy improvement amounts to $83.53\,\%$. As a matter of fact, the introduction of aiding information (e.g., the expected MTO trajectory) empowers the navigation filter against the detrimental GDOP conditions which are experienced along the MTO (see Fig. 1b for reference). Furthermore, these results have been obtained despite the adoption of an overly simple model to characterize the process dynamics between discrete-time filter iterations.

In addition, Fig. 3 highlights the convergence pattern (1σ-uncertainty) of the navigation filter estimates for the process states modelled in (12). Owing to high spacecraft dynamics, the process state estimate suffers the adoption of a constant velocity approximation (i.e., high acceleration noise). In turns, upon linearization of the state-transition model in the EKF, the gradient of $\boldsymbol{f}_{k-1}$ over the uncertainty bounds of the state-estimate is likely to be large. This condition, besides signalling a coarser model linearization against the one attainable with the true state, negatively impacts on the process state estimate. Moreover, such phenomenon reflects on the process covariance

TABLE I: Positioning error (m) for both plain EKF and TA-EKF architectures considering 3600 filter iterations at $1\,\mathrm{Hz}$.

Navigation Filter	Error Percentile (m)		
	50-th	75-th	95-th
Plain EKF	38.79	65.98	131.24
TA-EKF	4.32	8.52	21.61

estimate—which, as a consequence of linearization, depends upon the state estimate—and it is especially visible in Fig. 3b for the unaided EKF.

In light of the foregoing, the introduction of an aiding state as in the proposed TA-EKF empowers model linearization and leads to enhanced state estimates. Besides, the convergence pattern of covariance statistics improves accordingly.

V. Conclusions

By leveraging a dedicated simulation framework, the present study demonstrates the use of a customized EKF, i.e., TA-EKF to mitigate bad GNSS visibility conditions across MTOs. The filter exploits the trajectory data of a sample MTO to improve the EKF prediction stage. Under proper conditions this solution can improve the accuracy of the position estimate of about 84% at the 95-th percentile. Furthermore, the TA-EKF shows a faster convergence than its unaided counterpart in both position and velocity states. Further works will quantify the effects on the state estimation when inaccurate trajectory aidings are applied to the TA-EKF.

References

[1] W. P. Birmingham, B. L. Miller, and W. L. Stein, "Experimental Results of Using the GPS for Landsat 4 Onboard Navigation," *NAVIGATION*, vol. 30, no. 3, pp. 244–251, 1983, _eprint: https://onlinelibrary.wiley.com/doi/pdf/10.1002/j.2161-4296.1983.tb00843.x.

[2] T. G. Reid, T. Walter, P. K. Enge, D. Lawrence, H. S. Cobb, G. Gutt, M. O'Connor, and D. Whelan, "Navigation from Low Earth Orbit," in *Position, Navigation, and Timing Technologies in the 21st Century*. John Wiley & Sons, Ltd, 2020, pp. 1359–1379, section: 43 _eprint: https://onlinelibrary.wiley.com/doi/pdf/10.1002/9781119458555.ch43a.

[3] United Nations Office for Outer Space Affairs, "The interoperable global navigation satellite systems space service volume," *United Nations Digital Library*, pp. vii, 96 p. :, Oct 2018.

[4] J. L. Burch, T. E. Moore, R. B. Torbert, and B. L. Giles, "Magnetospheric Multiscale Overview and Science Objectives," *Space Science Reviews*, vol. 199, no. 1, pp. 5–21, Mar. 2016.

[5] O. Montenbruck, E. Gill, and F. Lutze, "Satellite orbits: models, methods, and applications," *Appl. Mech. Rev.*, vol. 55, no. 2, pp. B27–B28, 2002.

[6] L. Iess, M. Di Benedetto, N. James, M. Mercolino, L. Simone, and P. Tortora, "Astra: Interdisciplinary study on enhancement of the end-to-end accuracy for spacecraft tracking techniques," *Acta Astronautica*, vol. 94, no. 2, pp. 699–707, 2014.

[7] International Space Exploration Coordination Group (ISECG), "The Global Exploration Roadmap. Technical report, International Space Exploration Coordination Group (ISECG)," ISECG, Tech. Rep., 2018.

[8] E. Turan, S. Speretta, and E. Gill, "Performance analysis of crosslink radiometric measurement based autonomous orbit determination for cislunar small satellite formations," *Advances in Space Research*, 2022.

[9] A. Delépaut, A. Minetto, F. Dovis, F. Melman, P. Giordano, and J. Ventura-Traveset, "Enhanced GNSS-based positioning in space exploiting inter-spacecraft cooperation," in *Proceedings of the 2022 International Technical Meeting of The Institute of Navigation (ION ITM 2022)*, 2022, pp. 530–544.

[10] L. Musumeci, F. Dovis, J. S. Silva, P. F. da Silva, and H. D. Lopes, "Design of a High Sensitivity GNSS receiver for Lunar missions," *Advances in Space Research*, vol. 57, no. 11, pp. 2285–2313, Jun. 2016.

[11] V. Capuano, C. Botteron, J. Leclère, J. Tian, Y. Wang, and P.-A. Farine, "Feasibility study of GNSS as navigation system to reach the Moon," *Acta Astronautica*, vol. 116, pp. 186–201, 2015.

[12] N. Witternigg, G. Obertaxer, M. Schönhuber, G. B. Palmerini, F. Rodriguez, L. Capponi, F. Soualle, and J.-J. Floch, "Weak GNSS signal navigation for Lunar exploration missions," in *Proceedings of the 28th International Technical Meeting of the Satellite Division of The Institute of Navigation (ION GNSS+ 2015)*, 2015, pp. 3928–3944.

[13] M. Caceres Duran, P. Closas, E. Falletti, C. Fernández-Prades, M. Nájar, and F. Sottile, "Signal Processing for Hybridization," in *Satellite and Terrestrial Radio Positioning Technique*, D. Dardari, E. Falletti, and M. Luise, Eds. Oxford: Academic Press, 2012, ch. 6, pp. 317–382.

[14] J. Duník, S. K. Biswas, A. G. Dempster, T. Pany, and P. Closas, "State Estimation Methods in Navigation: Overview and Application," *IEEE Aerospace and Electronic Systems Magazine*, vol. 35, no. 12, pp. 16–31, Dec. 2020, conference Name: IEEE Aerospace and Electronic Systems Magazine.

[15] M. Murata, I. Kawano, and K. Inoue, "Simulation evaluation of moon transfer orbit navigation using gps carrier phases," in *Proceedings of the 34th International Technical Meeting of the Satellite Division of The Institute of Navigation (ION GNSS+ 2021)*, 2021, pp. 1033–1038.

[16] C. Mehlen and D. Laurichesse, "Improving GPS Navigation with Orbital Filter," in *Spacecraft Guidance, Navigation and Control Systems*, ser. ESA Special Publication, B. Schürmann, Ed., vol. 425, Feb. 2000, p. 123.

[17] E.-J. Choi, J.-C. Yoon, B.-S. Lee, S.-Y. Park, and K.-H. Choi, "Onboard orbit determination using GPS observations based on the unscented Kalman filter," *Advances in Space Research*, vol. 46, no. 11, pp. 1440–1450, Dec. 2010.

[18] V. Capuano, F. Basile, C. Botteron, and P.-A. Farine, "GNSS-based Orbital Filter for Earth Moon Transfer Orbits," *The Journal of Navigation*, vol. 69, no. 4, pp. 745–764, Jul. 2016, publisher: Cambridge University Press.

[19] R. Brown and P. Hwang, *Introduction to Random Signals and Applied Kalman Filtering with Matlab Exercises*, ser. CourseSmart Series. Wiley, 2012.

[20] O. Vouch, A. Minetto, G. Falco, and F. Dovis, "Enhanced Bayesian State Space Estimation for a GNSS/INS Tightly-Coupled Integration in Harsh Environment: An Experimental Study," in *34th International Technical Meeting of the Satellite Division of The Institute of Navigation (ION GNSS+ 2021)*, 2021, pp. 3368–3381.

[21] ——, "On the Adaptivity of Unscented Particle Filter for GNSS/INS Tightly-Integrated Navigation Unit in Urban Environment," *IEEE Access*, vol. 9, pp. 144 157–144 170, 2021.

[22] P. Groves, *Principles of GNSS, Inertial, and Multisensor Integrated Navigation Systems*, 2nd ed. 16 Sussex Street, London: Artech House, 2013.

[23] R. G. Brown and P. Y. Hwang, "Introduction to random signals and applied kalman filtering(book)," *New York, John Wiley & Sons, Inc., 1992. 512*, 1992.

[24] B.-K. Yi, H. Jagadish, and C. Faloutsos, "Efficient retrieval of similar time sequences under time warping," in *Proceedings 14th International Conference on Data Engineering*, 1998, pp. 201–208.

[25] Y. Guo, O. Vouch, S. Zocca, A. Minetto, and F. Dovis, "Enhanced EKF-Based Time Calibration for GNSS/UWB Tight Integration," *IEEE Sensors Journal*, vol. 23, no. 1, pp. 552–566, 2023.

[26] J. J. Parker, F. Dovis, B. Anderson, L. Ansalone, B. Ashman, F. H. Bauer, G. D'Amore, C. Facchinetti, S. Fantinato, G. Impresario *et al.*, "The Lunar GNSS Receiver Experiment (LuGRE)," in *Proceedings of the 2022 International Technical Meeting of The Institute of Navigation (ION ITM 2022)*, 2022, pp. 420–437.

[27] L. Konitzer, N. Esantsi, and J. Parker, "Navigation Performance Analysis and Trades for the Lunar GNSS Receiver Experiment (LuGRE)," in *2022 AAS/AIAA Astrodynamics Specialist Conference*, 8 2022.

[28] A. Minetto, F. Dovis, A. Nardin, O. Vouch, G. Impresario, and M. Musmeci, "Analysis of GNSS data at the Moon for the LuGRE project," in *2022 IEEE 9th International Workshop on Metrology for AeroSpace (MetroAeroSpace)*, Jun. 2022, pp. 134–139, iSSN: 2575-7490.

[29] W. A. Marquis and D. L. Reigh, "The GPS Block IIR and IIR-M Broadcast L-band Antenna Panel: Its Pattern and Performance," *NAVIGATION*, vol. 62, no. 4, pp. 329–347, 2015.

[30] J. E. Donaldson, J. J. Parker, M. C. Moreau, D. E. Highsmith, and P. D. Martzen, "Characterization of on-orbit gps transmit antenna patterns for space users," *NAVIGATION*, vol. 67, no. 2, pp. 411–438, 2020.

[31] W. Enderle, F. Gini, S. E., and M. V., "PROBA-3 Precise Orbit Determination based on GNSS Observations," in *32nd International Technical Meeting of the Satellite Division of The Institute of Navigation (ION GNSS+ 2019)*, 2019, pp. 1187–1198.

[32] P. Teunissen and O. Montenbruck, *Springer Handbook of Global Navigation Satellite Systems*, ser. Springer Handbooks. Springer International Publishing, 2021.